Journal of Nuclear Materials 525 (2019) 102–110

Contents lists available at ScienceDirect

Journal of Nuclear Materials

journal homepage: www.elsevier.com/locate/jnucmat

Evolution of B2 and laves phases in a ferritic steel under Fe^{2+} ion irradiation at 475 °C

Li He [a], [*], Lizhen Tan [b], Ying Yang [b], Kumar Sridharan [a]

[a] Department of Engineering Physics, University of Wisconsin-Madison, Madison, WI, 53706, USA
[b] Oak Ridge National Laboratory, One Bethel Valley Road, P.O. Box 2008, MS-6136, Oak Ridge, TN, 37831, USA

GRAPHICAL ABSTRACT

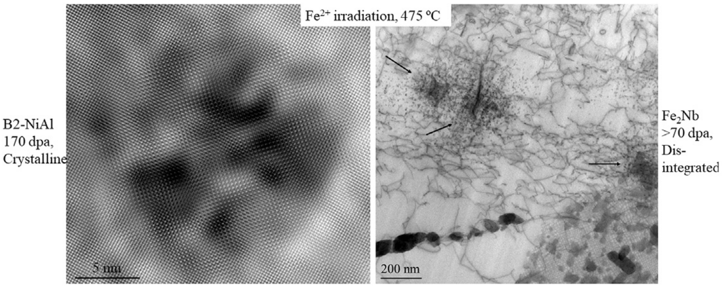

ARTICLE INFO

Article history:
Received 29 January 2019
Received in revised form
27 May 2019
Accepted 21 July 2019
Available online 22 July 2019

Keywords:
Ion irradiation
Ultrastrong steel
Ferritic steel
Microstructure
Precipitates
Transmission electron microscopy

ABSTRACT

Microstructural evolution in a novel ferritic steel (Fe–12Cr–3W–3Ni–3Al–1Nb, in wt.%) computationally designed to contain B2 and Laves phases after 4 MeV Fe^{2+} ion irradiation up to 220 dpa at 475 °C was characterized using transmission electron microscopy in conjunction with x-ray energy dispersive spectroscopy. The ferritic matrix phase exhibited dislocation loops and tangled dislocations, but our focus was on stability of two types of intermetallic precipitates. The B2–NiAl precipitates ~13 nm in size remained crystalline and appeared to have slightly lower Al concentration after irradiation. The Laves phase, $(Fe,Cr)_2(Nb,W)$, were present in two size ranges: coarse micron-scale precipitates which were amorphized with a slight composition change at irradiation doses above ~ 30 dpa, while the finer precipitate particles ~ 100 nm in size were partially disintegrated with a noticeable composition change at doses above ~ 70 dpa. Meanwhile, many Nb/Cr-enriched particles ~8 nm in size formed within a few hundreds of nanometers from the disintegrated particles. The understanding of the phase stability would help design advanced steels and engineer microstructures that are stable against high irradiation doses, while retaining good high temperature strength.

Published by Elsevier B.V.

1. Introduction

Advanced nuclear reactors require structural materials that can sustain neutron irradiation dose as high as 200 displacements per atoms (dpa) [1]. Developing alloys with nanoscale precipitate phases has been demonstrated to be a viable approach to both strengthen alloys and to also enhance radiation damage resistance by providing precipitate-matrix interfaces which serve as sinks for radiation-induced defects. Laves phases such as Fe_2W, Fe_2Mo and Fe_2Nb are common types of precipitates in ferritic and ferritic-

---

[*] Corresponding author.
E-mail address: Li.He@wisc.edu (L. He).

https://doi.org/10.1016/j.jnucmat.2019.07.024
0022-3115/Published by Elsevier B.V.

martensitic steels. While these phases beneficially impact the mechanical properties of steels, they do coarsen rapidly to sub-micrometer sizes despite their sluggish nucleation kinetics [2]. This coarsening impairs the steel's strength by way of increased inter-particle spacing and reduced solid solution strengthening owing to the loss of elements such as tungsten and molybdenum in matrix [3]. Introduction of high-density B2 precipitates (e.g., NiAl and FeAl) has led to the discovery of ultra-strong steels because of the minimal lattice misfit between the precipitates and ferritic matrix [4] and the non-shearable nature of such phases in an austenitic matrix [5]. However, the literature on the combined presence of B2 and Laves phase in ferritic alloys is scarce. The synergistic effect of B2 and Laves phases on the deformation behavior of a novel ferritic steel was investigated recently by one of the authors [6]. This study revealed that coherency change of B2 precipitates and development of ultrafine Laves phase could enhance creep resistance superior to the widely used T91 ferritic steel while the brittleness associated with coarse Laves phases could be mitigated by tuning the phase fraction [6]. However, the stability of Laves and/or B2 phases under radiation is not fully understood. Although Laves phase may undergo amorphization, compositional change, or dissolution under irradiation [7,8], further details on the nature of particle dissolution, and morphological and compositional changes of B2 phase particles are not well known. This work reports the evolution of Laves and B2 phases in a novel ferritic steel subjected to heavy ion irradiation at 475 °C up to ~220 dpa.

2. Material and methods

A ferritic steel (identified in this paper as BL-Nb) was designed using computational thermodynamics based on the CALPHAD (CALculation of PHAse Diagrams or Computer Coupling of Phase Diagrams and Thermochemistry) method using the JMatPro Fe-database to promote the formation of both Laves and B2 phase [9]. The alloy, with a nominal composition in weight percent (wt. %) Fe–12Cr–3W–3Ni–3Al–1Nb, was fabricated by vacuum arc-melting and casting into a bar in a size of 2.5 cm × 2.5 cm × 12 cm, followed by hot-rolling to 0.8 cm thick strip at 1000 °C after homogenization at 1200 °C for 15 min in an argon atmosphere. Finally, the material was aged at 650 °C for 5 h followed by air cooling to obtain equilibrium phase constituents. The calculated equilibrium precipitate phase compositions were $(Fe,Cr)_2(Nb,W)$ and Ni(Al,Nb) for the Laves and B2 phases, respectively, in a BCC ferritic matrix.

Samples of the alloy were polished to a mirror-like finish by grinding progressively with SiC paper to 1200 grit, followed by polishing with diamond paste down to 1 μm, and then finally with 0.1 μm silica colloidal solution. The samples were then ultrasonically cleaned in a methanol and alcohol bath. Ion irradiation of the samples was performed at the University of Wisconsin-Madison with a NEC 1.7 MV Tandem accelerator, using 4.0 MeV Fe^{2+} beam in a rastering mode to a fluence of 2.14×10^{17} ion/cm^2 at a flux of $(6.4 \pm 0.8) \times 10^{12}$ ion/cm^2/s. The irradiation was performed in the pressure range $2.6 \times 10^{-6} - 5.8 \times 10^{-7}$ Torr and the sample temperature was maintained at 474 ± 3 °C, averaged from two thermocouples attached to the opposite corners of the sample irradiation stage. This temperature was selected based on peak void swelling temperature of 450–480 °C reported for ferritic and ferritic-martensitic steels under ion irradiations [10–12]. Fig. 1 shows the simulated damage and implantation profiles of 4.0 MeV Fe^{2+} irradiation in the alloy BL-Nb, calculated using the Kinchin-Pease model in the Stopping and Range of Ions in Matter (SRIM) software [13]. The peak damage was 217 dpa at 1.11 μm depth with a peak damage rate of 6.5×10^{-3} dpa/s.

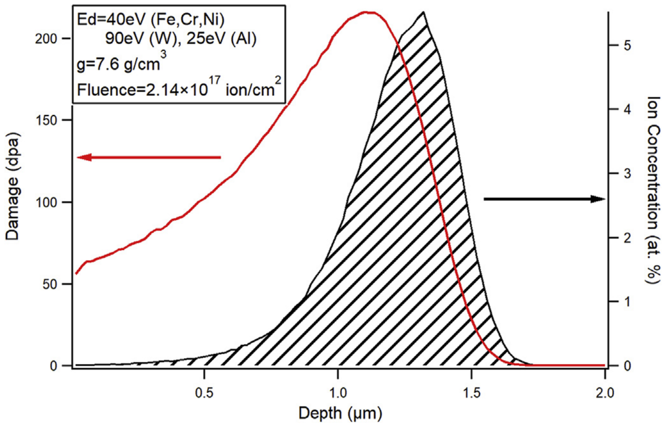

Fig. 1. 4.0 MeV Fe^{2+} induced damage and implantation profiles in the steel BL-Nb. *Ed* is atom displacement energy.

Specimens for transmission electron microscopy (TEM) characterization were prepared using focused ion beam (FIB: Zeiss Auriga). A 2 μm thick Pt protection layer was deposited at representative locations on the irradiated samples by electron beam and ion beam induced deposition, followed by 30 kV Ga^+ ion milling to produce lamellae of about 15 × 5 × 2 μm in size. The specimens were lifted out and attached to a TEM grid (procured from Ted Pella Inc.) and then thinned down to electron transparency sequentially with 30, 8, and finally 2 kV Ga^+ ions. TEM characterization was conducted with a FEI TF30 instrument at 300 kV, while scanning transmission electron microscopy (STEM) was conducted using a FEI Titan S-Twin aberration-corrected STEM equipped with an x-ray energy dispersive spectroscopy (EDS) at 200 kV with a typical electron beam semi-convergence angle of 24.5 mrad. The collection angle is typically 54–270 mrad for high angle annular dark field images (HAADF), and 6–13 mrad for annular bright field images (ABF). To form the HAADF image of ion irradiated B2 particles, a semi-convergence angle of 17.5 mrad and collection angle 143–717 mrad was applied to enhance the atomic number contrast. The sample thickness was measured from the intensity ratio between plasmon and zero-loss peaks in electron energy loss spectroscopy (EELS) under the following conditions: 200 kV electron energy, 24.5 mrad semi-convergence angle and 52 mrad collection angle. Size and number of B2–NiAl particles were measured manually from dark field images acquired with NiAl {001} diffraction spots.

TEM and STEM examination of the microstructure well below the irradiation depth was regarded as the base-line reference to evaluate irradiation damage effects at various depths below the surface within the irradiation depth. This also precludes the effects of any thermally-induced microstructural changes that may occur during the irradiation process.

Accurate evaluation of precipitate composition by EDS analysis is generally compromised by the surrounding matrix because of the common overlap of particle and matrix. The following method was utilized for particle compositional analysis to exclude interference effects from the matrix. If the composition of an element in a particle and matrix are C_p and C_m, respectively, and the thicknesses of the particle and matrix are t_p and t_m, the average composition of the particle within the matrix is:

$$\overline{C} = \frac{C_p t_p + C_m t_m}{t_p + t_m} \tag{1}$$

Let $t_p + t_m = 1$. If the elements are present only in the particle but not matrix, i.e., $C_m = 0$, then

$$\overline{C} = C_p t_p \tag{2}$$

or if the elements are not present in the particle,

$$\overline{C} = C_m t_m = C_m(1 - t_p) \tag{3}$$

Otherwise,

$$C_p = \frac{\overline{C} - C_m(1 - t_p)}{t_p} \tag{4}$$

C_m is measured from the matrix area adjacent to the particles. Assuming stoichiometric particle composition, e.g., 33.3 atomic percent (at. %) Nb in Fe_2Nb, C_p is known for elements present only in particles. Then t_p can be calculated from (2). If elements are known not to exist in precipitate particles, t_p can be calculated from (3). The rest of elemental compositions in the particle are calculated from (4). The method was applied to analyze particles with either one or combination of a few elements having a fixed composition (with assumption of stoichiometry), or major component elements known to be absent from particles to obtain reliable t_p. In addition, non-metal components (e.g., C, N) were evaluated with EDS peak intensities rather than calculated compositions because of the reduced EDS sensitivity for light elements.

3. Results

3.1. B2–NiAl phase

Fig. 2 shows B2 precipitates in the unirradiated region of the sample. The dark-field (DF) TEM image in Fig. 2a was taken from a [100] zone axis with one of the NiAl {001} spots as shown in the inset, which reveals the B2 phase as bright particles, < 20 nm in size, uniformly dispersed in the matrix. The diffraction pattern indicates the coherency between the B2 phase (simple cubic with one element on the corner and the other element in the body center) and the BCC matrix. The higher magnification HAADF image in Fig. 2b shows the B2 particles in dark shade with a white peripheral halo. The HAADF contrast suggests low-Z (mass) nature of the B2 particles, which is confirmed by its Ni and Al enrichment from the EDS line scan (Fig. 2c) across a representative B2 particle pointed by an arrow in Fig. 2b. Compositional values of Cr and W fluctuate near zero inside the particle possibly due to small particle size (t_p in equation (3)) compared to the sample thickness. Averaging the concentration of seven B2 particles yielded Ni (50.7 ± 1.6) – Al (44.7 ± 1.4) – Fe (4.6 ± 0.9) in atomic percent. Scattered minor enrichment in Nb was observed at particles' center, which is consistent with the thermodynamically calculated composition of Ni(Al,Nb) type B2 phase. B2 particles show a periphery of white contrast in HAADF images and dark contrast in ABF images (not shown here), indicating strain at the particle/matrix interface.

The structure of B2–NiAl particles after Fe^{2+} ion irradiation at 475 °C is shown in Fig. 3. The cross-sectional regions at depth of 0.15–0.6 μm and 1.15–1.6 μm, corresponding to about 68–115 dpa and 210–10 dpa according to Fig. 1, respectively, are shown in Fig. 3a and b. The top side of the images is close to the irradiated surface. The micrographs were imaged using the $\{001\}_{NiAl}$ reflection from the [100] zone axis as shown in the inset of Fig. 3a. The irradiation did not alter the crystallinity of the B2 phase particles. Some coarser particles are seen in the top part of Fig. 3a from 0.15 to ~0.3 μm depth, which might be influenced by irradiation surface effects [14,15]. Unlike limited solubility of Ni, Al has considerable solubility (~2.1 wt % at 475 °C from thermodynamic considerations) in the matrix. The coarsening of the NiAl particles in the near surface region might have been facilitated by the enhanced aluminum diffusivity because of the increased vacancy production in this region by irradiation cascades [16]. Therefore, the near surface region (<~0.3 μm) has not been studied in general. The average size of B2–NiAl particles in the region encompassing 0.3–0.6 μm depth was characterized to be 11.3 ± 0.2 nm with number density of $1.5 \times 10^{22}\ m^{-3}$ in Fig. 3a (~81–115 dpa), which suggests that the particles experienced slight diminution and an increase in number density compared to that in the unirradiated condition (Fig. 2a) where the corresponding values were, 12.3 ± 0.1 nm and $9.3 \times 10^{21}\ m^{-3}$, respectively. In contrast, the B2–NiAl particles appeared with lower contrast at a greater depth of 1.15–1.3 μm (at the top part of Fig. 3b) corresponding to the range from peak damage to peak implanted Fe according to Fig. 1. Beyond this, B2–NiAl particle size increased to 14.0 ± 0.2 nm, which is larger than that in the unirradiated region, and with number density of $7.1 \times 10^{21}\ m^{-3}$. Fig. 3c shows a high-resolution HAADF image of a B2–NiAl particle, taken along the [100] zone axis illustrated in the inset for a fast Fourie transform (FFT) of the original image, at depth of 0.86 μm where the damage level was about 170 dpa. The HAADF image was smoothed, together with an applied mask to emphasize atomic columns, which shows Ni columns in a brighter contrast compared to the neighboring Al inside the particle. All the columns of the particle aligned well with the matrix planes, verifying full coherency between the irradiated particle and matrix. The wavering contrast in the particle and matrix was induced by local strains.

EDS-measured composition of the irradiated B2–NiAl particles is shown in Fig. 4. Linear fit of fifteen particles' composition vs. damage level was performed and the fitting parameters are listed in legends. Although data are scattered, they appear to show a trend of increasing Ni and decreasing Al with damage level. This may be a

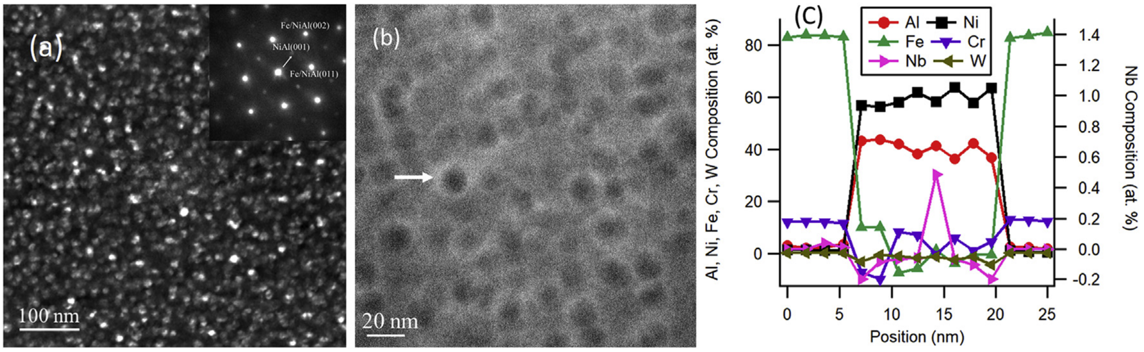

Fig. 2. B2–NiAl precipitates in the unirradiated region: (a) DF-TEM image from the [100] zone acquired with one of the $\{001\}_{NiAl}$ diffraction spots as indicated in the electron diffraction pattern of the inset, (b) HAADF image, and (c) EDS line scan compositional profiles across the particle pointed by the arrow in (b).

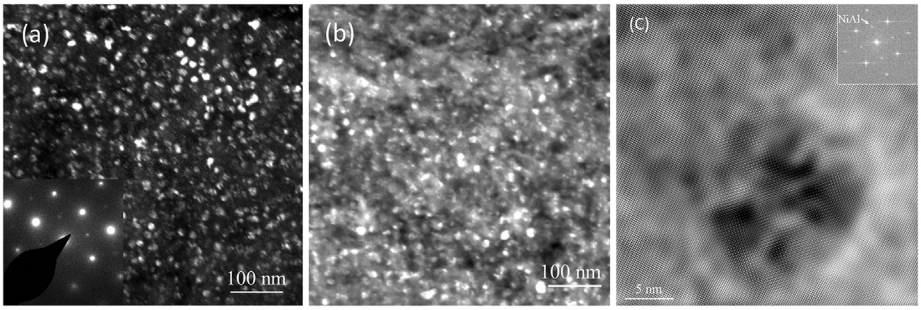

Fig. 3. Images of B2–NiAl particles in the irradiated region: DF-TEM images at (a) 0.15–0.6 μm depth and (b) 1.15–1.6 μm depth. The images were taken with the $\{001\}_{NiAl}$ diffraction from the [100] zone axis as shown in the inset of (a); (c) HAADF image at 0.86 μm from surface with the inset of an FFT of the original image.

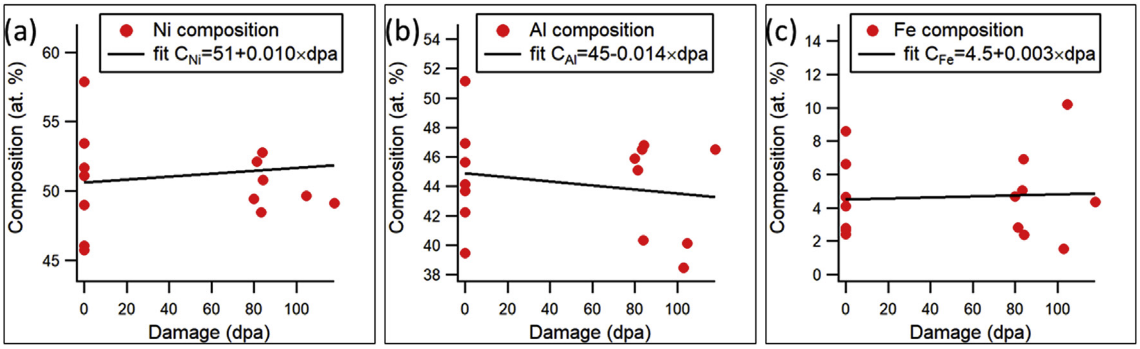

Fig. 4. EDS measured composition of B2–NiAl phase particle as a function of irradiation damage: (a) Ni, (b) Al, (c) Fe.

result of lower Al diffusivity than Ni in B2–NiAl, as discussed later, leaving higher concentration of irradiation-induced Al vacancies, $V_{Al} > V_{Ni}$, or more Ni antisites $Ni_{Al} > Al_{Ni}$ in B2. One the other hand, the slight increase of Fe composition with damage appears to coincide with implanted Fe concentration rise (~0.25 at. % at 120 dpa).

3.2. Laves phase

Fig. 5a shows the cross sectional image of the sample after Fe^{2+} ion irradiation up to 220 dpa at 475 °C. The irradiation resulted in a surface damage layer with a depth of 1.8 μm, slightly larger than the SRIM calculated 1.7 μm damage depth as shown in Fig. 1. No apparent voids were found in the sample after irradiation. Coarse micron-scale particles were occasionally observed in the sample, primarily inside grains, while many finer particles in about 100 nm size range were dispersed with higher densities at grain boundaries and in some domains within grains, and in both the unirradiated and irradiated regions. The domains had dense mesh-type dislocations (shown later in the lower-right corner of Fig. 7a), favoring the particle precipitation. Fig. 5b shows an ABF image at a higher magnification from the unirradiated region taken from the boxed region in the lower left corner of Fig. 5a to illustrate the small particles interacting with short dislocations. Nanobeam electron diffraction pattern from particle-A and EDS line scan profiles across particle-B in Fig. 5b, both in the undamaged region, are shown in Fig. 5c and d, respectively, confirming the particles to be Laves phases. Particle-A is a Fe_2Nb-like crystalline phase, coherent with matrix with an orientation relationship of $<011>_{Particle\text{-}A}//<100>_{Matrix}$, $(100)_{Particle\text{-}A}//(01\bar{1})_{Matrix}$, and $(\bar{1}2\bar{2})_{Particle\text{-}A}//(011)_{Matrix}$. Particle-B has a composition of Fe (55.4 ± 3.4) – Cr (11.9 ± 1.9) – Nb (21.4 ± 2.1) – W (11.3 ± 1.8) (at. %), suggesting a Laves phase $(Fe,Cr)_2(Nb,W)$.

Irradiation damage of a coarse micron-scale Laves phase particle is shown in Fig. 6, where half of the particle is within the irradiated region (and the other half is in the unirradiated region) provides a distinct contrast to visualize radiation effect on Laves phase. The points labelled A and B exist in the lightly damaged (<20 dpa, 1.6 μm depth) and heavily damaged (190 dpa, 0.96 μm) regions, respectively, on the particle where nanobeam electron diffraction were taken. The lightly damaged part of the particle shows a Fe_2Nb $<42\bar{3}>$ diffraction pattern, while the heavily damaged part is an amorphous ring pattern yielding a darker contrast than the crystalline part in the ABF image. Similar amorphous ring patterns were also observed in the center dark region above A. Amorphization is usually accompanied by a volume change, resulting in local strains. However, TEM did not reveal noticeable strain contrast at the adjacent region. The inclined phase boundary between the Laves and matrix that is clearly shown in the (lower part) crystalline region disappears in the (upper part) amorphous region. EDS line scan profiles across the particle from the unirradiated to the irradiated region are shown in Fig. 5b, which confirms the Laves particle to be $(Fe,Cr)_2(Nb,W)$. Composition of the particle is Fe (59.6 ± 0.6) – Cr (7.1 ± 0.6) – Nb (26.6 ± 0.2) – W (6.6 ± 0.2) (at. %) for the crystalline part, and Fe (59.7 ± 0.3) – Cr (7.1 ± 0.3) – Nb (26.2 ± 0.3) – W (7.0 ± 0.3) (at. %) for the amorphous part. Irradiation seems to slightly increase W content which may be attributable to the radiation-enhanced diffusivity favoring more W precipitation from solid solution. Compared to the finer Laves phase particle characterized in Fig. 5d, the coarse Laves phase particle had noticeably higher Nb and Fe and with less W and Cr. This is reasonable because the coarse Laves phase is believed to form at higher temperatures during the hot-rolling process than the finer Laves phase formed during the aging process. Nb has significantly lower solubility in Fe compared to W and Cr, resulting in preferential Nb enrichment for the coarse Laves phase particles

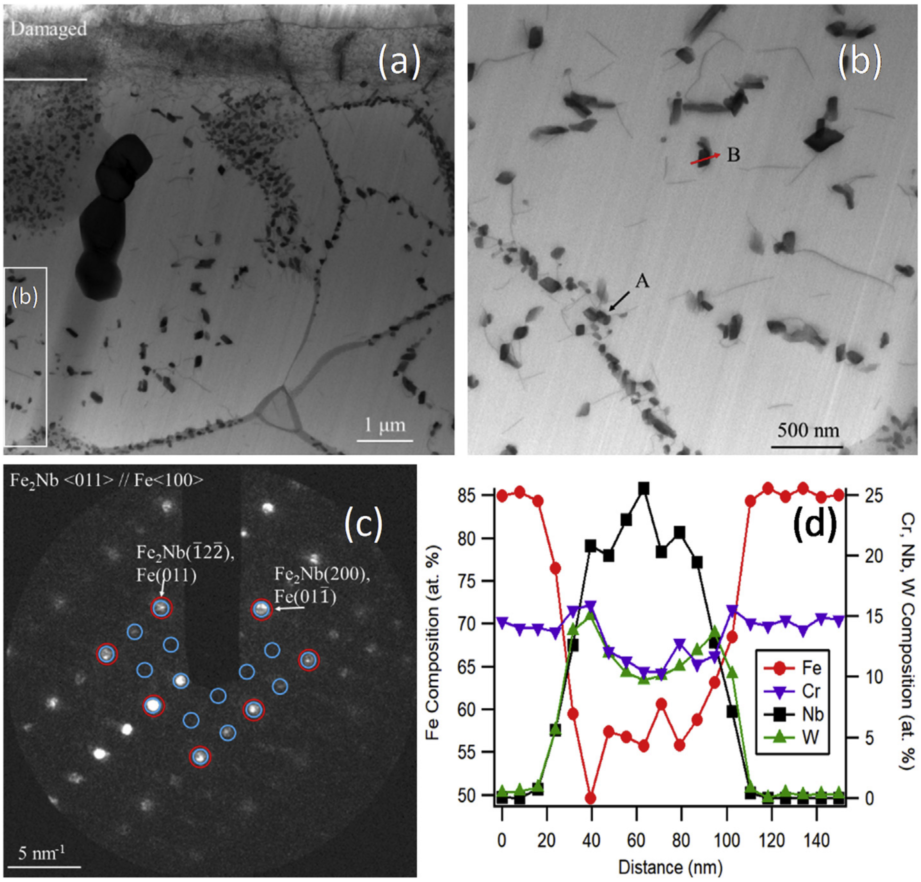

Fig. 5. (a, b) ABF cross-sectional images along [100] zone of the irradiated BL-Nb sample showing Laves phase precipitates. (a) Top region is damaged. End of the damage depth is indicated by the white line. (b) Undamaged Laves phase precipitates. (c) nanobeam electron diffraction of particle identified as A shown in (b). Red and blue circles indicate matrix and particle-A diffraction spots, respectively. (d) EDS compositional profiles across particle-B shown in (b). Both particles are undamaged. (For interpretation of the references to colour in this figure legend, the reader is referred to the Web version of this article.)

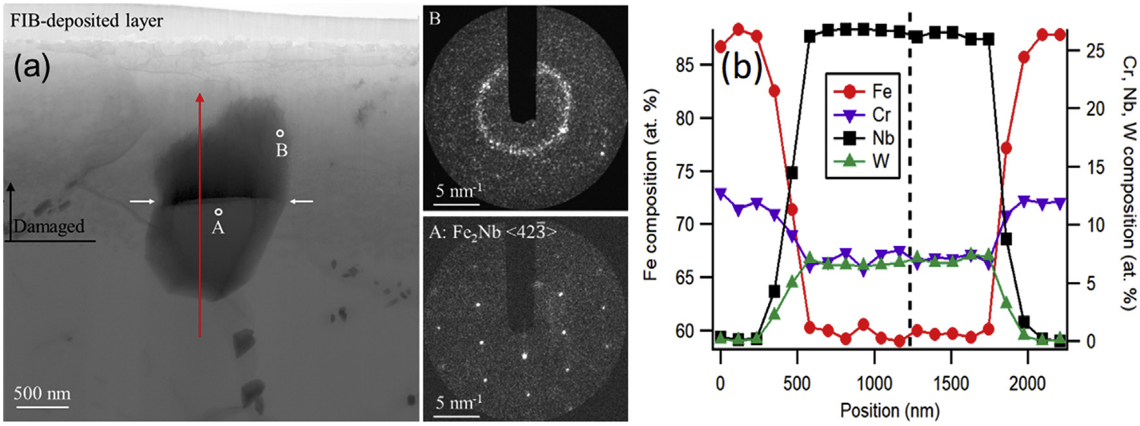

Fig. 6. (a) ABF image of a coarse Laves phase particle that spans across the irradiated region into the unirradiated region and corresponding nanobeam electron diffraction patterns from the regions labelled A and B. The contrast line inside the particle, as indicated by two short white arrows, is at 1.5 μm depth (~30 dpa) near the end of damage range. (b) EDS line scan profiles along the red arrow line in (a), with a vertical dashed line indicating the interface of the ABF contrast line on the particle. (For interpretation of the references to colour in this figure legend, the reader is referred to the Web version of this article.)

formed at higher temperatures. The boundary of crystalline/amorphous regions, indicated by the short white arrows in Fig. 6a and the vertical dashed line in Fig. 6b, is at 1.5 μm depth where damage level is about 30 dpa, which may imply that this may be amorphization threshold for this type of Laves phase. The peak implanted Fe with a value of ~5.5 at. % is expected to be at ~200 nm right from the vertical dashed line according to Fig. 1, which does not appear to influence the particle composition.

The higher magnification cross-sectional ABF images of the irradiated region are shown in Fig. 7a and b, where the centers of these images are at depths of 1.2 and 0.83 μm, respectively. The imaging location of Fig. 7b is the boxed region in Fig. 7a. The

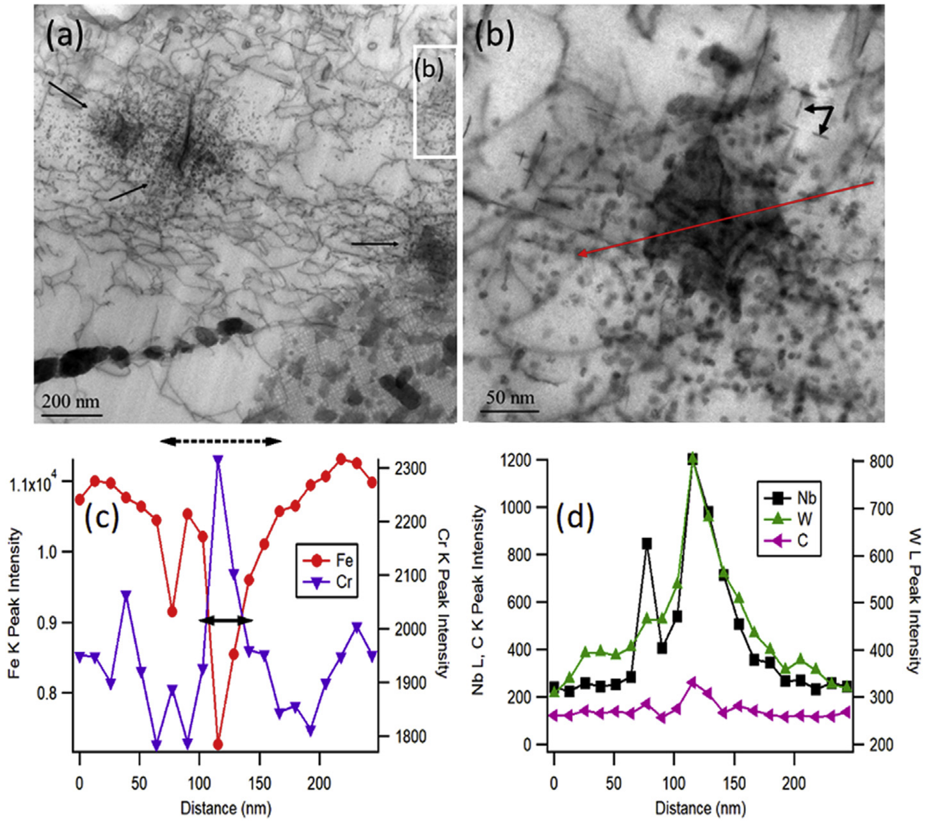

Fig. 7. Radiation-induced disintegration of finer Laves phase particles: ABF images along [100] zone with the center of the images at (a) 1.2 μm depth, about 200 dpa, and (b) 0.83 μm depth, about 164 dpa. Black arrows in (b) indicate examples of dislocation loops. (c, d) EDS line scan profiles along the red arrow across the damaged particle in (b). Dashed and solid arrows in (c) indicate widths of particle and core, respectively. (For interpretation of the references to colour in this figure legend, the reader is referred to the Web version of this article.)

damage levels at the image centers are about 200 and 164 dpa, respectively, according to the SRIM calculation in Fig. 1. Compared to the unirradiated matrix shown in Fig. 5b, the irradiation primarily induced tangled dislocations with some dislocation loops. Based on the shapes of dislocation loops and their orientation relationships with the *g*-vectors under the <100> zone [17], both ½<111> and <100> types of loops are identified in Fig. 7a. Here the ½<111> type loops are in an oval shape with the elongated axis perpendicular to the <011> orientation, while the <100> type loops are in a sharp short-line shape as shown in Fig. 7a and b with the length perpendicular to the <100> orientation (<100> dislocation loops are indicated by black arrows in Fig. 7b). More tangled dislocations appear at higher doses (deeper region close to the peak damage and implantation), while dislocation loops primarily form at lower doses (closer to the irradiated surface), which suggest a dose-dependent evolution of dislocations. Statistical quantitative analyses of the dislocations and loops were not pursued in this work as the primary focus was on the evolution of the two types of precipitates.

The three particles indicated by arrows in Fig. 7a do not have distinctive phase boundaries, unlike the undamaged particles in the lower part of the image. The particles are surrounded by many nanometer-scale fine precipitates, which are more clearly exemplified in Fig. 7b. EDS line scan profiles were collected across the particle in Fig. 7b following the red arrow line, which are shown in Fig. 7c and d, revealing the damaged particle with a width of ~130 nm and a core width of ~50 nm. The core is enriched with Cr, Nb, W, and a minor amount C, indicative of the original composition of Laves phase, $(Fe,Cr)_2(Nb,W)$. The particle was disintegrated by irradiation, with the Nb, W components diffusing into surrounding matrix. However, Cr peak intensity at core periphery (at distance of 60–90 nm and 160–190 nm in Fig. 7c) is lower than that in the surrounding matrix (at distance of 0–50 nm and 200 nm and beyond), suggesting Cr may diffuse from particle periphery into the core. Such a disintegration of the fine Laves phase particles was observed at doses greater than ~70 dpa (≥~0.2 μm depth).

3.3. New phases around damaged finer laves phase

As demonstrated in Fig. 7a and b the finer Laves particles exhibited radiation damage. Many nanometer-sized precipitates were observed surrounding these damaged Laves phase particles, which extended over a few hundreds of nanometers from the center of the Laves phase particles. Fig. 8a shows an ABF image of such precipitates adjacent to a damaged Laves phase particle, where the damage level is about 180 dpa at the center of the image. The particles generally had an elongated oval shape with a length of ~8 nm. EDS line scan profiles across a particle denoted by a red arrow line in Fig. 8a, is shown in Fig. 8b, which indicate that this fine particle is composed of Nb, Cr, N and C. Fig. 8c shows a high-resolution HAADF image of such a particle along matrix [100] axis at about 150 dpa. Two major atomic column plane spacings in the particle were characterized to be 0.30 nm and 0.26 nm with 55° between the planes, suggesting MX phases NbC/NbN <110> or Z-phase CrNbN <221>. Combined with the EDS analysis in Fig. 8b, the nanometer-sized precipitates are identified to be CrNb(N,C)-type Z-phase. Z-phase is not a thermodynamically stable phase in this alloy system and forms due to non-equilibrium conditions induced

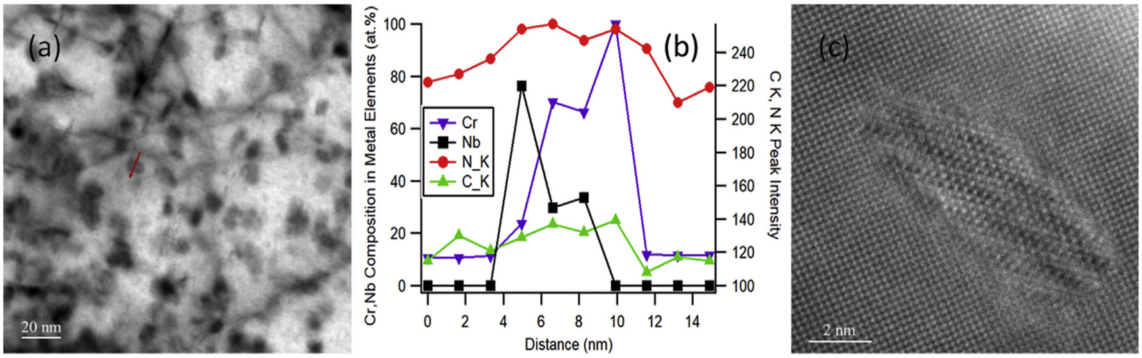

Fig. 8. Precipitates formed after irradiation: (a) ABF image at 0.9 μm depth corresponding to damage of 180 dpa. (b) EDS line scan profiles along the red arrow in (a), of Cr, Nb atomic percentages in metal components (i.e., Fe, Cr, Nb) and C—K, N—K peak intensity. (c) HAADF image of a particle at 0.78 μm depth corresponding to a damage of 150 dpa. (For interpretation of the references to colour in this figure legend, the reader is referred to the Web version of this article.)

by ion irradiation. Additionally, both nitrogen and carbon are not alloying elements and were controlled to be as low as possible (on the order of 50 ppm by weight or less) during arc-melting of the alloy. EDS line scan from surface to a few microns deep indicated significant C and N intensity from surface to about 0.3 μm depth, about twice that of the background intensity. The C and N intensity then gradually decreased with depth till around 2 μm (near the end of damage depth) and was stable at deeper regions. The result shows ion irradiation introduced C and N into the sample, as reported in other studies [18,19]. This may have caused the precipitation of Z-phase particles around disintegrated Laves phase.

4. Discussion

Coarsening of NiAl-type precipitates under thermal aging has been observed in ferritic steels with kinetics following a cubic rate law of $\bar{r} = kt^{1/3}$ with $\bar{r}$ is the mean particle radius, t is the aging time, and k as a constant [20,21]. Coarsening of NiAl particles to 50 ± 10 nm from initial 11 ± 2 nm was also observed in creep-ruptured ferritic steel samples with a composition similar to BL-Nb, when tested at 650 °C for 119 h [6]. Extrapolation of the coarsening kinetics to lower temperatures [20] suggests that the thermal effect for 9 h irradiation at 475 °C would lead to negligible coarsening (~2.8 nm). The slightly smaller particle size observed in the irradiated region (depth of 0.3—0.6 μm in Fig. 3a: 11.3 ± 0.2 nm) compared to the unirradiated region (Fig. 2a: 12.3 ± 0.1 nm) might suggest a slight radiation-induced partial dissolution of the NiAl particles. However, thermodynamic calculations for the alloy, as shown in Fig. 9a suggests an increase of NiAl mole fraction at 475 °C by ~36% from the initial material aged at 650 °C, which implies the possibility of radiation-induced precipitation of new NiAl particles that manifested as lower average particle size. To achieve conclusive results, further detailed statistically significant quantitative studies are needed. Additionally, the implanted Fe was estimated to be up to ~5.5 at. % at the peak implantation depth ~1.3 μm from surface according to Fig. 1, which increases the Fe content up to 77.45 at.% from initial 76.2 at.%. Such a small increase (up to 1.25 at. %) in Fe content would noticeably reduce the amount of Cr-rich BCC phase, but only slightly reduce (or destabilize) B2 and Laves phases as suggested by the predictions in Fig. 9b. Therefore, the implanted Fe would have only a secondary effect on the stability of B2 and Laves phases in terms of alloy thermodynamics. Radiation-induced defects evolution and enhanced diffusion would be the primary factors governing the phase stability.

Laves phase $(Fe,Cr)_2(Nb,W)$ particles in two sizes were present in the alloy BL-Nb before irradiation. The fate of the Laves phase particles during irradiation depends on their sizes. Coarse micron-scale particles became amorphous at irradiation doses above ~30 dpa, while small particles in ~100 nm disintegrated to even finer sizes. Besides amorphization, irradiation also resulted in slight compositional changes of the Laves phase compared to the unirradiated crystalline phase, as shown in Fig. 6b. However, finer Laves

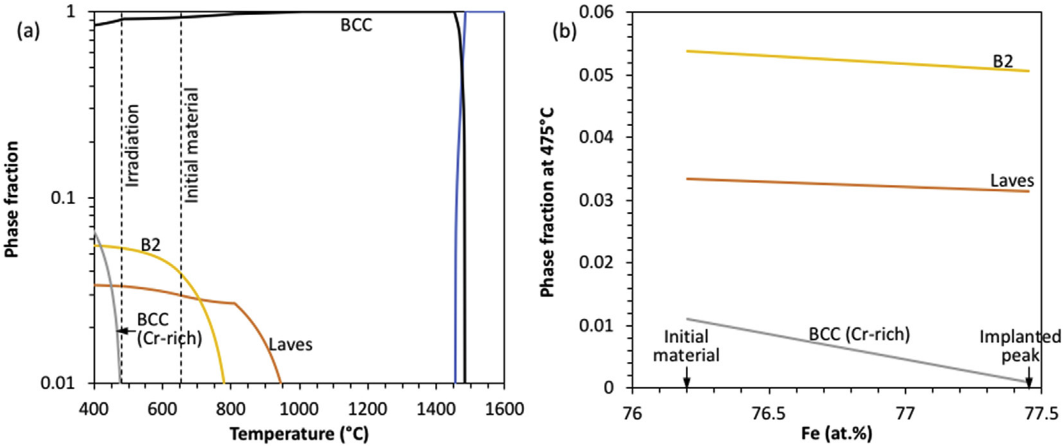

Fig. 9. Thermodynamic predictions for alloy BL-Nb: (a) temperature-dependent phase mole fraction and (b) effect of implanted Fe on phase mole fraction at 475 °C (with the BCC phase > 0.9 mol fraction).

phase particles lost their original composition integrity as shown in Fig. 7c and d (irradiated) compared to Fig. 5d (unirradiated). Taylor et al., reviewed $(Fe,Cr)_2Zr$ Laves phase in Zircaloy. Under neutron irradiation Fe diffuses out of the $(Fe,Cr)_2Zr$ particle periphery, causing the crystalline core to shrink and finally amorphize [22]. A similar process might have occurred for the fine Laves particles in the ferritic steel BL-Nb investigated in this study. Irradiation induced outward diffusion of Nb and W at the periphery of the fine $(Fe,Cr)_2(Nb,W)$ particles with inward diffusion of Cr and C as shown in Fig. 7c and d. Thermal annealing may recover radiation-induced amorphization and slight composition changes experienced by the coarse Laves phase. However, the finer Laves particles experienced irreversible compositional change and disintegrated because of their larger surface-to-volume ratio.

The initial alloy precipitates B2–NiAl and Laves are the equilibrium phases at 650 °C, which would increase in sizes or densities if aged at 475 °C for a long time as suggested in Fig. 9a, considering the sluggish kinetics at such a low temperature. Under irradiation, the excessive defect concentration on one hand could enhance the diffusion kinetics, aiding the system reach equilibrium faster, and on the other hand, the excessive defect concentration could lead to disordering or even amorphization of ordered crystalline phases. Compared to the relatively stable B2–NiAl particles with small enrichment in Ni and depletion in Al, Laves phase experienced noticeable degradation under irradiation. One reason for the variation in irradiation stability of the two phases might be their crystal structures. B2–NiAl has a cubic lattice with a Pearson symbol of cP2, while the Laves phase $(Fe,Cr)_2(Nb,W)$ is a tetrahedrally close-packed phase having a hexagonal lattice with a Pearson symbol of hP12. The complex unit cell structure, tending to have a more limited homogeneity range with less tolerance for composition ranges, may cause the Laves phase to be more prone to losing its long-range order and eventually amorphize under irradiation. Atomistic simulations have indicated that self-diffusion in stoichiometric or Ni-rich NiAl is dominated by the mechanism of next-nearest-neighbor (NNN) vacancy jumps [23]. Diffusion of Al by this mechanism is likely to occur more slowly with a higher activation energy than diffusion of Ni, e.g., 3.557 (D_{NiAl}^{Al}) vs. 2.428 eV (D_{NiAl}^{Ni}) [23,24], which are slightly higher than the diffusion activation energies of Al and Ni in BCC-Fe which are 2.228 and 2.259 eV, respectively [25,26]. Although similar data are not available for Laves phase, Mehrer reviewed self-diffusion coefficients of B2–NiAl and Laves Fe_2Ti [27], which revealed that the self-diffusion coefficient of B2–NiAl is one order of magnitude higher than that of Laves Fe_2Ti in the same temperature range. Therefore, while the diffusion in B2–NiAl is comparable to that in the matrix, the diffusion in Laves $(Fe,Cr)_2(Nb,W)$ is much slower, leading to the greater propensity for amorphization of Laves phase compared to B2–NiAl.

5. Conclusions

Samples of a ferritic alloy (Fe–12Cr–3W–3Ni–3Al–1Nb) were irradiated with 4.0 MeV Fe^{2+} up to 220 dpa at 475 °C. The radiation-induced microstructural evolution was characterized by TEM in conjunction with EDS. Radiation induced the formation of dislocation loops at lower doses and tangled dislocations at higher doses, however the primary focus of this work was on the phase and compositional stability of two types of precipitates, namely, B2–NiAl and Laves phase $(Fe,Cr)_2(Nb,W)$. B2–NiAl precipitates remained crystalline and fully coherent with matrix under irradiation, with slight size diminution, number density increase, and compositional change (slightly more enriched in Ni) at the irradiation depth of 0.3–0.6 μm (80–115 dpa) compared with unirradiated B2–NiAl. The alloy contains both coarse micron-scale and fine (~100 nm) Laves phase particles. The coarse Laves phase particles were amorphized under irradiation along with a slight compositional change at damage levels greater than ~30 dpa. In contrast, disintegration of the finer Laves particles was observed to occur at damage levels greater than ~70 dpa (≥~0.2 μm depth). The disintegration resulted in a noticeable compositional change and also in the nucleation of many new ultra-fine particles ~8 nm in size, identified to be CrNb(N,C)-type Z-phase, which precipitated in the vicinity of the disintegrated finer Laves phase particles.

Acknowledgments

The authors gratefully acknowledge the support of U.S. Department of Energy, Office of Nuclear Energy, a Nuclear Energy Enabling Technologies FY2015 Award, under Contract no. DE-AC05-00OR22725. The authors also acknowledge use of facilities and instrumentation supported by NSF through the University of Wisconsin Materials Research Science and Engineering Center (DMR-1720415).

References

[1] S.J. Zinkle, L.L. Snead, Designing radiation resistance in materials for fusion energy, Annu. Rev. Mater. Res. 44 (1) (2014) 241–267.
[2] A. Schneider, G. Inden, Simulation of the kinetics of precipitation reactions in ferritic steels, Acta Mater. 53 (2) (2005) 519–531.
[3] F. ABe, Effect of fine precipitation and subsequent coarsening of Fe_2W laves phase on the creep deformation behavior of tempered martensitic 9Cr-W steels, Metall. Mater. Trans. A 36 (2) (2005) 321–332.
[4] S. Jiang, et al., Ultrastrong steel via minimal lattice misfit and high-density nanoprecipitation, Nature 544 (2017) 460.
[5] S.-H. Kim, H. Kim, N.J. Kim, Brittle intermetallic compound makes ultrastrong low-density steel with large ductility, Nature 518 (2015) 77.
[6] T. Chen, et al., High-temperature strengthening mechanisms of Laves and B2 precipitates in a novel ferritic alloy, Mater. Sci. Eng., A 720 (2018) 110–116.
[7] H. Tanigawa, et al., Radiation induced phase instability of precipitates in reduced-activation ferritic/martensitic steels, J. Nucl. Mater. 367–370 (2007) 132–136.
[8] G. Kobylyansky, et al., Irradiation-induced growth and microstructure of recrystallized, cold worked and quenched zircaloy-2, NSF, and E635 alloys, J. ASTM Int. (JAI) 5 (4) (2008) 1–19.
[9] T.C. Ying Yang, Lizhen Tan, Computational Thermodynamics Aided Design of Novel Ferritic Alloys, oak ridge national laboratory, 2016 vol. ornl/tm-2016/229.
[10] M.B. Toloczko, et al., Ion-induced swelling of ODS ferritic alloy MA957 tubing to 500dpa, J. Nucl. Mater. 453 (1) (2014) 323–333.
[11] J.G. Gigax, et al., Radiation response of alloy T91 at damage levels up to 1000 peak dpa, J. Nucl. Mater. 482 (2016) 257–265.
[12] E. Aydogan, et al., Effect of self-ion irradiation on the microstructural changes of alloy EK-181 in annealed and severely deformed conditions, J. Nucl. Mater. 487 (2017) 96–104.
[13] J.F. Ziegler, M.D. Ziegler, J.P. Biersack, SRIM – the stopping and range of ions in matter, Nucl. Instrum. Methods Phys. Res. Sect. B Beam Interact. Mater. Atoms 268 (11) (2010) 1818–1823, 2010.
[14] G.S. Was, et al., Emulation of reactor irradiation damage using ion beams, Scr. Mater. 88 (2014) 33–36.
[15] S.J. Zinkle, L.L. Snead, Opportunities and limitations for ion beams in radiation effects studies: bridging critical gaps between charged particle and neutron irradiations, Scr. Mater. 143 (2018) 154–160.
[16] R.E. Stoller, The effect of free surfaces on cascade damage production in iron, J. Nucl. Mater. 307–311 (2002) 935–940.
[17] B. Yao, D.J. Edwards, R.J. Kurtz, TEM characterization of dislocation loops in irradiated bcc Fe-based steels, J. Nucl. Mater. 434 (1) (2013) 402–410.
[18] J.G. Gigax, et al., Beam-contamination-induced compositional alteration and its neutron-atypical consequences in ion simulation of neutron-induced void swelling, Mater. Res. Lett. 5 (7) (2017) 478–485.
[19] G.S. Was, et al., Resolution of the carbon contamination problem in ion irradiation experiments, Nucl. Instrum. Methods Phys. Res. Sect. B Beam Interact. Mater. Atoms 412 (2017) 58–65.
[20] H. Calderon, M.E. Fine, Coarsening kinetics of coherent NiAl-type precipitates in Fe-Ni-Al and Fe-Ni-Al-Mo alloys, Mater. Sci. Eng. 63 (2) (1984) 197–208.
[21] Z. Sun, et al., Nano-sized precipitate stability and its controlling factors in a NiAl-strengthened ferritic alloy, Sci. Rep. 5 (2015) 16081.
[22] D.F. Taylor, H.R. Peters, W.J.S. Yang, A simple kinetic model of zircaloy Zr(Fe,Cr)2 precipitate amorphization during neutron irradiation, in: S. Bruemmer, P. Ford, G. Was (Eds.), Ninth International Symposium on Environmental Degradation of Materials in Nuclear Power Systems—Water Reactors, The Minerals, Metals & Materials Society, 1999, pp. 1161–1168.

[23] Y. Mishin, D. Farkas, Atomistic simulation of point defects and diffusion in B2 NiAl, Philos. Mag. A 75 (1) (1997) 169–185.
[24] S. Yu, et al., Self-diffusion in the intermetallic compounds NiAl and Ni3Al: an embedded atom method study, Phys. B Condens. Matter 396 (1) (2007) 138–144.
[25] T. Helander, J. Ågren, A phenomenological treatment of diffusion in Al–Fe and Al–Ni alloys having B2-b.c.c. ordered structure, Acta Mater. 47 (4) (1999) 1141–1152.
[26] B. Jönsson, Assessment of the mobilities of Cr, Fe and Ni in bcc Cr-Fe-Ni alloys, ISIJ Int. 35 (11) (1995) 1415–1421.
[27] H. Mehrer, Diffusion in intermetallics, Mater. Trans., JIM 37 (6) (1996) 1259–1280.